FULL PAPER

Earth atmospheric loss through the plasma mantle and its dependence on solar wind parameters

Audrey Schillings[1,2]* , Rikard Slapak[3], Hans Nilsson[1,2], Masatoshi Yamauchi[1], Iannis Dandouras[4] and Lars-Göran Westerberg[5]

Abstract

Atmospheric loss and ion outflow play an important role in the magnetospheric dynamics and in the evolution of the atmosphere on geological timescales—an evolution which is also dependent on the solar activity. In this paper, we investigate the total O^+ outflow $[s^{-1}]$ through the plasma mantle and its dependency on several solar wind parameters. The oxygen ion data come from the CODIF instrument on board the spacecraft Cluster 4 and solar wind data from the OMNIWeb database for a period of 5 years (2001–2005). We study the distribution of the dynamic pressure and the interplanetary magnetic field for time periods with available O^+ observations in the plasma mantle. We then divided the data into suitably sized intervals. Additionally, we analyse the extreme ultraviolet radiation (EUV) data from the TIMED mission. We estimate the O^+ escape rate [ions/s] as a function of the solar wind dynamic pressure, the interplanetary magnetic field (IMF) and EUV. Our analysis shows that the O^+ escape rate in the plasma mantle increases with increased solar wind dynamic pressure. Consistently, it was found that the southward IMF also plays an important role in the O^+ escape rate in contrast to the EUV flux which does not have a significant influence for the plasma mantle region. Finally, the relation between the O^+ escape rate and the solar wind energy transferred into the magnetosphere shows a nonlinear response. The O^+ escape rate starts increasing with an energy input of approximately 10^{11} W.

Keywords: O^+ outflow/escape, Plasma mantle, Solar wind, Interplanetary magnetic field (IMF), Extreme ultraviolet (EUV), Coupling functions

Introduction

The Sun plays an important role in terrestrial atmospheric loss. It is believed that billions of years ago, the Sun was more active than today. Enhanced particle fluxes and solar radiation affected the planetary environment and may have led to significant atmospheric losses (Güdel 2007). Thus, the Earth's atmospheric loss is an important phenomenon which may affect the evolution of the atmosphere on geological timescales. This terrestrial phenomenon is driven, at lower altitudes ($\sim$ 2 Earth radius [Re]), by atmospheric ions energised to a few eV and photoelectrons called the polar wind (Axford 1968; Nagai et al. 1984; Green and Waite 1985; Chappell et al. 1987; Chandler et al. 1991; Yau et al. 2007). At higher altitudes ($> 2Re$), highly energised—up to a few keV—heavy ions, such as oxygen ions (O^+), are flowing upward (Shelley et al. 1982). Those O^+ ions are heated through different processes, such as field-aligned currents (Maggiolo et al. 2006) at lower altitudes or perpendicular heating via wave–particle interactions (Bouhram et al. 2004b; Slapak et al. 2011; Waara et al. 2011; Nilsson et al. 2012) at higher altitudes. Once the upward moving ions have sufficient energy to escape the gravity, they become ion outflow. The latter are further accelerated under the curvature of the magnetic field lines, called centrifugal acceleration (Nilsson et al. 2008, 2010). The main regions where we observe outflowing ions are the open magnetic

Schillings *et al. Earth, Planets and Space*   (2019) 71:70

Page 2 of 13

field line regions: the polar cap, cusp and plasma mantle. The polar cap represents the mapping of the open field lines to the ionosphere, whereas the cusp is a funnel between the dayside closed magnetic field lines and the open magnetic field lines. This funnel provides a direct entry for magnetosheath plasma into the magnetosphere. The plasma mantle located downstream of the cusp has a mixed plasma population of ionospheric and magnetosheath ions. It is, however, dominated by solar wind ions conducted by the mirror force. In the part of the magnetotail, Wang et al. (2014b) found that the plasma mantle is characterised by similar temperature as in the magnetosheath and lower density, namely ~ 0.05–0.2 keV and ~ 0.1–1 cm^{-3}. The area and size of the three regions are influenced by strong solar wind conditions, and it results in fluctuations of the penetrating solar wind. Several studies have been conducted in different magnetospheric regions to determine how the solar wind affects the O^+ outflow (e.g Palmroth et al. 2001; Abe et al. 1996; Denton and Taylor 2008; Gou et al. 2016).

The global low-energy ion outflow (dominated by H^+, not O^+) has been studied under one solar cycle by André et al. (2015). The authors found that during one solar cycle, the increasing extreme ultraviolet (EUV) radiations ($F_{10.7}$ a proxy for EUV flux) increase the outflow by a factor 2. They explained this enhancement by a higher density in the outflowing population and concluded that the available ionospheric ion density limits the outflow mechanism. Those low-energy ions can gain energy through solar illumination which changes the ionospheric scale height (Maes et al. 2015). However, according to Li et al. (2018) the energy transfer efficiency of the solar wind is 6–7 orders of magnitude higher than the energy originating from the solar illumination. Solar illumination of the polar cap is much affected by the tilt of the geomagnetic dipole. In another study, Li et al. (2017) studied this aspect combined with the $F_{10.7}$ flux and found that the cold ion outflow is strongly influenced by the dipole tilt angle and the EUV flux. In a similar way, Engwall et al. (2009) showed an increase in the cold ion outflow (up to 60 eV) with $F_{10.7}$ and concluded that EUV radiation mainly controls the low-energised ion density.

Some cold ions are further energised to become a hot plasma population observed in the cusp, and they are either accelerated further to the plasma mantle and escape directly into the magnetosheath (Slapak et al. 2013) or transported to the plasma sheet (Kronberg et al. 2014; Liao et al. 2015). The density of those energetic O^+ ions observed in the plasma sheet is strongly influenced by the geomagnetic (Kp) and solar (EUV) activity

(Mouikis et al. 2010; Maggiolo and Kistler 2014; Kistler and Mouikis 2016).

The O^+ outflow dependence on the interplanetary magnetic field (IMF) has been observed in the dayside magnetosheath and magnetopause regions (Slapak et al. 2012; Marcucci et al. 2004). However, in the high-altitude polar cap, Elliott et al. (2001) did not found any correlation between IMF and O^+ density in contrast to Lennartsson et al. (2004) who considered the same region but for O^+ outflow. The latter found that the total O^+ outflow rate was approximately three times higher for southward IMF ($B_z < 0$) than for northward IMF. Despite all these studies on different solar wind parameters related to O^+ outflow, the plasma mantle has not been well analysed. The plasma mantle was well sampled by the Cluster mission and is suitable to study ions that are likely to escape from the magnetosphere. Thus, this study aims to answer how the O^+ escape rate from the plasma mantle depends on the solar wind dynamic pressure, IMF, EUV and solar wind energy input.

Instrumentation and data

For our data analysis, we used oxygen ion data provided by the Cluster mission (see "Cluster data" section) and solar wind data (see "Solar wind data" and "TIMED data" sections) in order to establish the correlation between O^+ flux and the solar wind.

Cluster data

The Cluster mission (Escoubet et al. 2001) was launched in 2000 and has collected magnetospheric data for more than 18 years. Four spacecrafts are flying in tetrahedral formation on a polar elliptical orbit and carry 11 identical instruments each. One of the instruments is the COmposition DIstribution Function (CODIF) included in the Cluster Ion Spectrometer (CIS) (Rème et al. 2001) that provides a 3-D distributions of ion data, with mass discrimination through a time-of-flight section. With this technique, it can measure H^+, He^{2+}, He^+ and O^+. CODIF has a 360° field of view, an energy coverage from 25 eV/q (per charge) up to 40 keV/q and an energy resolution of $\Delta E/E \sim 0.16$.

The magnetic field data were taken from the FluxGate Magnetometer (FGM) (Balogh et al. 2001). The instrument has a normal mode sample frequency of 22.4 Hz and operative ranges for different magnetic intensities from a few nT to several thousand of nT. However, we only used the averaged magnetic field over the spacecraft spin (4 sec).

Solar wind data

The solar wind data, such as velocity, density and interplanetary magnetic field (IMF), were retrieved from the

Schillings *et al. Earth, Planets and Space*   (2019) 71:70

Page 3 of 13

OMNIWeb online database. This NOAA/SWPC database is a collection of solar data from several satellites with various scientific objectives at diverse positions. The plasma parameters and IMF are provided by IMP8, Wind, Geotail and ACE. In our study, we used the high-resolution data, 5 min and 1 min, time-shifted to the Earth's bow shock.

TIMED data

The extreme ultraviolet (EUV) data are taken from the SEE instrument on board TIMED (Thermosphere, Ionosphere, Mesosphere Energetics and Dynamics) mission (Kusnierkiewicz 2003). TIMED was launched in December 2001 and has so far collected 17 years of data. It has a circular orbit with an inclination of $74.1°$ and an orbital period of 97 min and carries four sensors. One of these is the Solar EUV Experiment (SEE) (Woods et al. 2000) designed to measure and determine the rates of energy deposition, dissociation and ionisation of solar FUV (Far Ultraviolet), EUV and soft X-ray irradiance from 1 to 195 nm and with a 0.5-nm spectral resolution. The Sun is observed a few minutes ($\sim$ 3 min) during each orbit and an average value is determined, which gives 14–15 measurements per day.

Data set criteria

Our data set consists of 5 years of solar wind and Cluster data (from 2001 to 2005) and 4 years (as the mission started 1 year later) of EUV data (2002–2005). Our reason not to include more data is to focus on the oxygen data dependency on solar wind parameters without including a potential solar cycle dependency. The resolutions of the data for Cluster, solar wind and EUV are approximately 4 s, 1 min and 97 min, respectively, as well as a 0.5-nm spectral resolution for the wavelength of EUV irradiance.

In the Cluster data set, some of the O^+ counts might be false due to high flux proton contamination. Those ions typically originate from the intense magnetosheath fluxes, and they occur as a background in the O^+ mass channel. Such contamination typically leads to underestimated O^+ velocity moments. The false counts have a similar energy distribution as the protons, so for only false counts, the O^+ perpendicular bulk velocity will be 1/4 smaller than the proton velocity, and this can be used to identify cases with significant contamination; see Nilsson et al. (2006) for more details about the method. About 20% of data with significant background counts are removed from our data set. However, these data correspond mainly to magnetosheath data (which we do not want in our data set), and even if the percentage of removed data is high, this does not affect our O^+ occurrence rate in the plasma mantle (see "Method" section).

In order to analyse O^+ data from the plasma mantle, some conditions are consequently implemented to remove magnetosheath, cusp and polar cap data. The polar cap is usually associated with low-energy ions in contrast to the plasma mantle composed mainly of energetic solar particles, meaning these two regions can be distinguished by the ratio between the thermal pressure and the magnetic pressure called the plasma β. In the polar cap, plasma β is typically around 0.05 and consequently our constraint is $\beta > 0.1$ to avoid polar cap data (see e.g. Liao et al. 2010, 2015; Haaland et al. 2017). Moreover, several studies, such as Nilsson et al. (2006), Kistler et al. (2006), Slapak et al. (2017), have shown that the plasma sheet and plasma mantle populations have similar plasma β but can be distinguished by their density and temperature. Thus, we excluded the plasma sheet population by setting the proton perpendicular temperature to $T_\perp(H^+) < 1750$ eV. The density constraints are $n(H^+) > 10^{-3}$ cm^{-3} and $10^{-3} < n(O^+) < 100$ cm^{-3} to guarantee reliable bulk velocity estimates. The inner magnetosphere is removed by an arbitrary spatial constraint that still has a significant latitudinal and dawn–dusk coverage an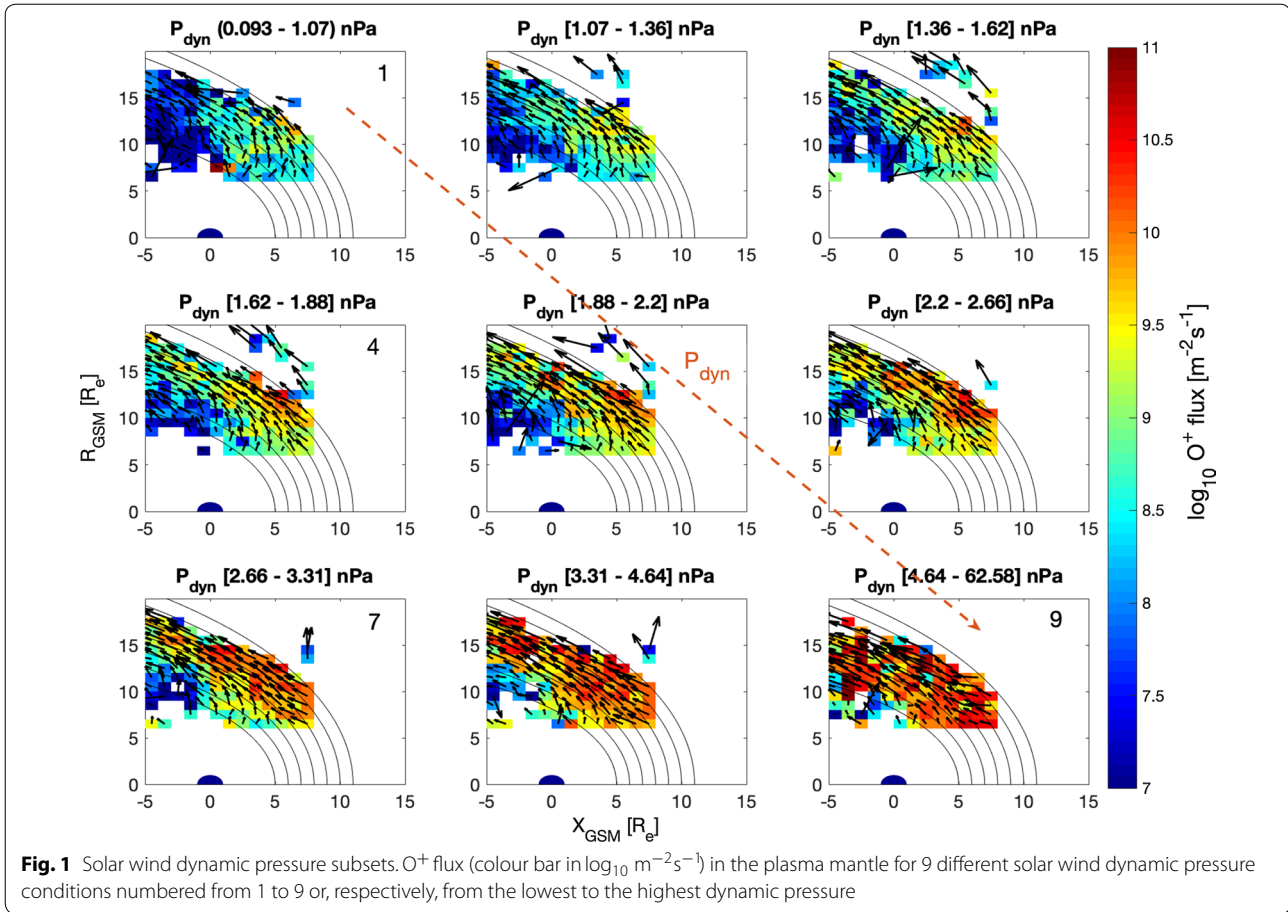d defined in cylindrical coordinates as $R_{GSM} = \sqrt{Y_{GSM}^2 + Z_{GSM}^2} > 6\,R_e$ and $-5 < X_{GSM} < 8\,R_e$. To avoid cusp data, we set $v_\parallel(H^+) > 0$ because most of the proton outward flux is observed in the plasma mantle. In practice, $v_\parallel(H^+)$ is mostly positive, and thus, only a few observations are removed by this conditions. Magnetosheath data are removed by the cross-talk condition (false background counts). These conditions lead to a data set containing only plasma mantle data. Finally, we define the O^+ outflow in the plasma mantle as the local flux with an outward flux and therefore $v_\parallel(O^+) > 0$ km/s.

Data from some major geomagnetic storms are removed from our data set since they turn out to correspond to other magnetospheric regions than the plasma mantle (Schillings et al. 2017). Those events are 29 Oct 2003 (full day), 7 and 9 Nov 2004 (full days), 4 Dec 2003 (from 20:00 to 00:00 UT) and 13 Sep 2004 (from 20:00 to 00:00 UT).

Interpolation

The solar wind data provided by the OMNIWeb online database have 1-min resolution while Cluster data have 4 s. Therefore, two interpolations have been done on the solar wind data: The first one removes the values set at 999.999 in the database corresponding to *no measured values*, and the second one interpolates the solar wind data to the Cluster data points. The interpolations use a nearest neighbour interpolation

Schillings *et al. Earth, Planets and Space*   (2019) 71:70

Page 4 of 13

Fig. 1 Solar wind dynamic pressure subsets. O^+ flux (colour bar in $\log_{10}$ m^{-2}s^{-1}) in the plasma mantle for 9 different solar wind dynamic pressure conditions numbered from 1 to 9 or, respectively, from the lowest to the highest dynamic pressure

technique. The same procedure is applied to the TIMED data for EUV.

Method

This section describes how we analysed the total O^+ escape [s^{-1}] from the plasma mantle under different solar wind conditions.

Solar wind dynamic pressure and interplanetary magnetic field

Based on previous studies of ion escape at Mars by Ramstad et al. (2015, 2017), we first looked at the solar wind velocity and density distributions. We divided these distributions into 9 solar wind subsets, with approximately the same amount of observations in each. The O^+ outflow (net outward flux) is calculated for the 9 subsets. However, analysis of these 9 subsets indicated that we could use the dynamic pressure instead. We therefore chose to not use exactly the same method as used for Mars, even though this was our original intention. It appears that the parameters and conditions to determine outflow at Earth or at Mars differ.

The solar wind dynamic pressure in Pa is given by

$$P_{\text{dyn}} = m_{\text{SW}} \cdot n_{\text{SW}} \cdot v_{\text{SW}}^2 \tag{1}$$

where $m_{\text{SW}} \cdot n_{\text{SW}}$ is the solar wind mass density in kg/m^3 and v_{SW} the solar wind velocity in m/s. We then divided P_{dyn} equally (approximately same amount of data points) in an increasing order to obtain 9 new solar wind subsets. Following the same method as Slapak et al. (2013, 2017), we estimated the O^+ flux (in the plasma mantle) for these 9 subsets shown in Fig. 1. In Fig. 1, the average O^+ fluxes is represented in 1 Re × 1 Re bins by the colour bar showing the O^+ flux in logarithmic scale. Note that the bins are only a representation of our data and are not used in the O^+ flux calculations (see Eq. 2 below). The small black arrows associated with the O^+ flux correspond to the average bulk velocity direction in each bin. The six black curves, referred to as *layer* hereafter, are magnetopause-like curves based on the Shue model (Shue et al. 1998) and are used to divide the plasma mantle region into layers. They contribute to the total escape flux estimate (see explanation below). Furthermore, the 9 subplots display the 9 P_{dyn} subsets from the lowest values (top left, number 1) to the highest P_{dyn} values (bottom right, number 9), also illustrated with an orange dashed arrow. The P_{dyn}

intervals for each subset are given in the title of the sub-plots in nPa.

Afterwards, the total O^+ escape was calculated for the 9 P_{dyn} subsets. These steps are described below and summarised by Eq. 2.

First, for each layer i (or between two magnetopause-like segments), we defined the total escape flux $f_{esc,i}(O^+)$ $[s^{-1}]$ as the average O^+ flux $f_{mean,i}(O^+)$ $[m^{-2}\ s^{-1}]$ estimated in the layer times the layer area A_i. The area is given by $A_i = 0.59 \cdot \pi \cdot (r_{i+1}^2 - r_i^2)$ [Re] taken from Slapak et al. (2013) where the factor 0.59 comes from a 106° wide angle in the ZY_{GSE} plane containing most of the O^+ observations. Additionally, the first magnetopause-like segment is plotted at $r_1 = 5$ Re, so that $r_i = 4 + i$ [Re].

For the second step, we considered how often O^+ is observed in the layer ($N_i(O^+)$) compared to the total number of observations in the layer ($N_{tot,i}$). This parameter is called the occurrence rate and defined as $N_i(O^+)/N_{tot,i}$. The second step gave us the total escape O^+ flux for each layer $F_{esc,i}(O^+)$.

Finally, the third step was an addition of the layers as shown in the last line of Eq. 2 to obtain the total O^+ escape flux $F_{tot}(O^+)$ from the plasma mantle. Thus, we get $F_{tot}(O^+)$ for the 9 subplots corresponding to different solar wind dynamic pressure conditions.

$$\text{step 1:} f_{esc,i}(O^+) \quad [s^{-1}] = f_{mean,i}(O^+) \cdot A_i \tag{2a}$$

$$\text{step 2:} F_{esc,i}(O^+) \quad [s^{-1}] = f_{esc,i}(O^+) \cdot \frac{N_i(O^+)}{N_{tot,i}} \tag{2b}$$

$$\text{step 3:} F_{tot}(O^+) \quad [s^{-1}] = \sum_i F_{esc,i}(O^+) \tag{2c}$$

We also investigated the relation between the total O^+ escape rate and IMF through the clock angle given by $\theta = \arctan(|B_{Y,IMF}|/|B_{Z,IMF}|)$. A similar method was applied: division of the parameter in an increasing order and estimate of the total O^+ escape flux for the 9 subsets through the tree steps described above.

Solar wind coupling functions

Since the solar wind dynamic pressure contains only density and velocity and not IMF, we looked at solar wind coupling functions such as the epsilon or Akasofu parameter (Akasofu 1981) and a derivative of the epsilon parameter, the Vasyliunas et al. formula (Vasyliunas et al. 1982). Koskinen and Tanskanen (2002) give a physical review in a modern context and clarifications how to use the Akasofu parameter with correct units. They described ϵ as a rate of solar wind energy that empowers the magnetosphere. The Koskinen formula of the epsilon parameter in SI units reads

$$\epsilon \ [W] = \frac{4\pi}{\mu_0} \cdot v_{SW} \cdot B_T^2 \cdot \sin^4(\theta/2) \cdot l_0^2 \tag{3}$$

where $\mu_0 = 4\pi \times 10^{-7}$ [kg m/A^2 s^2] is the vacuum permeability, v_{SW} [m/s] is the solar wind velocity, $B_T = \sqrt{B_Y^2 + B_Z^2}$ [T] is the transverse IMF, θ [rad] is the clock angle and $l_0^2 = 49$ [R$_e^2$] is the effective area of the solar wind–magnetosphere interaction (Akasofu 1981). However, the epsilon parameter is usually used for geomagnetic storms and a few hours, not years of data (Finch and Lockwood 2007; Tenfjord and Østgaard 2013; Wang et al. 2014a).

Thus, we also implemented three variations of the Vasyliunas et al. formula. The original formula (Vasyliunas et al. 1982) describing the rate of solar wind energy that enters the magnetosphere is given by

$$\begin{aligned} P_\alpha \ [W] = M_E^{2/3} &\cdot \mu_0^{(1/3-\alpha)} \cdot m_{SW}^{(2/3-\alpha)} \\ &\cdot n_{SW}^{(2/3-\alpha)} \cdot v_{SW}^{(7/3-2\alpha)} |B|^{2\alpha} F(\theta) \end{aligned} \tag{4}$$

where $M_E = 8.06 \times 10^{22}$ [A/m^2] is the Earth's magnetic dipole moment, μ_0 the vacuum permeability, $m_{SW} \cdot n_{SW}$ [kg/m^3] the mass density, v_{SW} [m/s] the velocity, $|B|$ the IMF [T], $F(\theta)$ a function of the clock angle and finally α, a coupling function that can be found empirically. The function $F(\theta)$ is commonly defined as sinus of the clock angle and α has different values within the literature, e.g. Murayama (1982), Stamper et al. (1999), Finch and Lockwood (2007), Tenfjord and Østgaard (2013), Wang et al. (2014a). In our study, one variation of the Vasyliunas et al. formula is the original one (Eq. 4) with the coupling coefficient $\alpha = 0.3$ from Finch and Lockwood (2007). Note that we did not use the author's formula but only their α value (see Additional file 1 for more details). For the second variation, we used a coupling coefficient $\alpha = 0.5$ from Tenfjord and Østgaard (2013). The authors defined energy coupling functions for storms and long time series. In our study, we took their long time series formula (see Additional file 1: Eq. 1 for more details). The third variation was taken from Wang et al. (2014a), who made 240 simulations and found $\alpha = 0.43$ and $F(\theta) = \sin(\theta/2)^{2.7} + 0.25$. We also used the original authors equation (see Additional file 1: Eq. 3 for more details). As before, the coupling functions were divided in 9 approximately equal subsets (same amount of data points in each division) where we estimated the total O^+ escape rate. The four coupling functions and how O^+ escape depends on them were then investigated; see "Observations and results" section.

Extreme ultraviolet radiation

The EUV irradiance is provided by the SEE instrument on board TIMED (see "Instrumentation and data" section for more details). In this study, we used the observational average that consists of about 15 measurements

Schillings *et al. Earth, Planets and Space* (2019) 71:70

Page 6 of 13

per day. In these measurements, only the wavelengths absorbed by O^+ ($\lambda = 10$–90 nm) are of interests. The total EUV intensity I_{tot} including these wavelengths $I(\lambda)$ is calculated as

$$I_{\text{tot}} = \int I(\lambda) d\lambda \simeq \sum_{n=\lambda}^{\lambda_{\text{end}}} I(\lambda) \Delta\lambda \qquad (5)$$

where $\Delta\lambda = 1$ [nm] is the bin of the wavelength. Afterwards, the total EUV intensity was interpolated on the Cluster data for the years 2002–2005. In order to look at the correlation between EUV and the total O^+ escape flux, the EUV intensity values were also sorted in increasing order and equally distributed in 9 subsets. Furthermore, the EUV intensity was divided in *Low EUV* and *High EUV* according to its mean value 0.0035 W/m^2.

Another way to express the EUV correlation with the total O^+ escape flux is to estimate the photoionisation flux (see "Discussion" section). The latter is defined by the EUV intensity $I(\lambda)$ divided by the photon energy E_γ as

$$F(\lambda) = \frac{I(\lambda)}{E_\gamma(\lambda)} \quad \text{with} \quad E_\gamma(\lambda) = \frac{hc}{\lambda}$$
$$F_{\text{tot}} = \int F(\lambda) d\lambda \simeq \sum_{n=\lambda}^{\lambda_{\text{end}}} F(\lambda) \Delta\lambda \qquad (6)$$

where h and c are the Planck constant and speed of light, respectively. Like all others parameters, the photoionisation flux was equally distributed in 9 subsets for which we calculated the total O^+ escape flux.

Observations and results

We hereby present the correlation between the total O^+ escape flux and the solar wind parameters described in "Method" section.
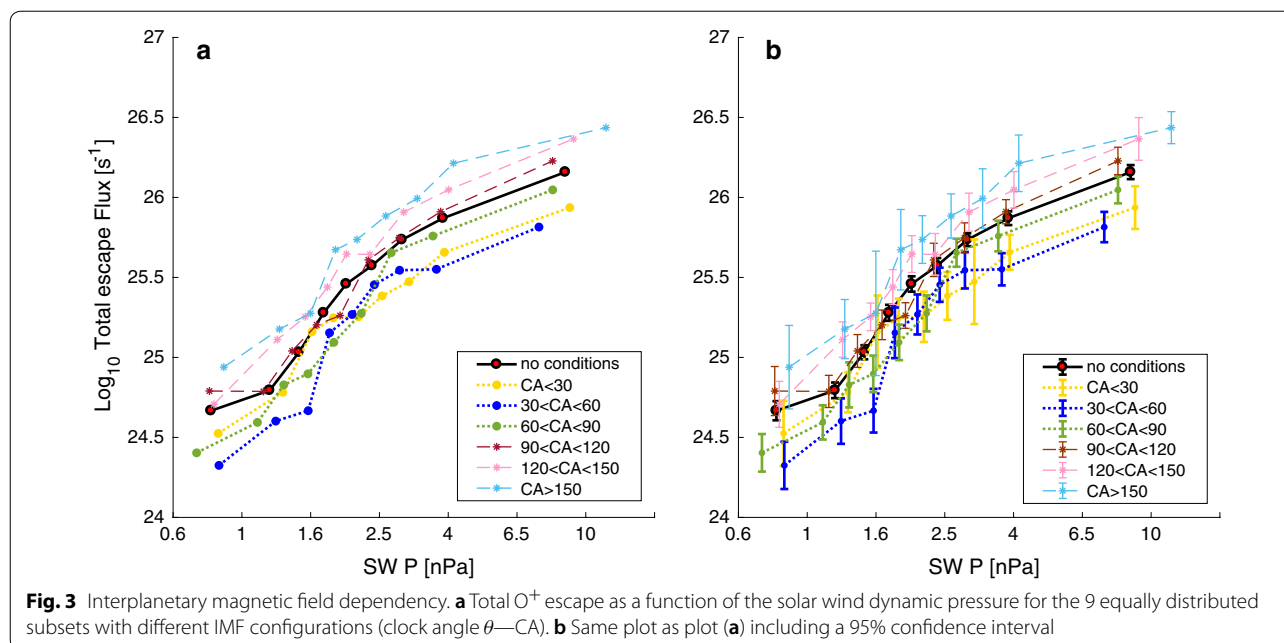
Solar wind dynamic pressure and IMF

The solar wind density and velocity were first investigated individually; however, these two parameters can be coupled by taking the solar wind dynamic pressure P_{dyn} (see Eq. 1). After dividing P_{dyn} into 9 ascending subsets, Fig. 1 shows the O^+ outflow for each subset. An enhancement of approximately 1.5 order of magnitude is observed for the O^+ flux between the subsets of lowest and highest solar wind dynamic pressure. The O^+ outflow for the lowest P_{dyn}, first subset (Fig. 1, subplot nb. 1 top left) has an upper limit of 2.78×10^9 m^{-2} s^{-1} (with a minimum of 5% observations in the bin), whereas for the higher P_{dyn}, last subset (Fig. 1, subplot nb. 9 bottom right) we already see visually an enhancement of the O^+ outflow. The latter has an upper limit of 8.84×10^{10} m^{-2} s^{-1} (with a
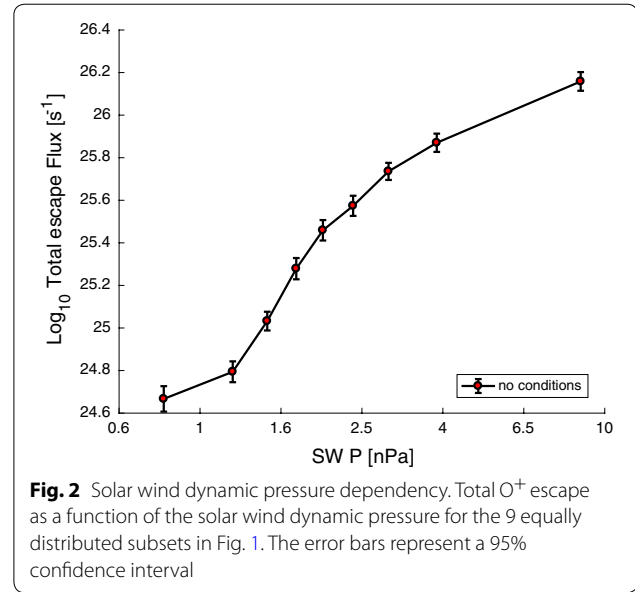
Fig. 2 Solar wind dynamic pressure dependency. Total O^+ escape as a function of the solar wind dynamic pressure for the 9 equally distributed subsets in Fig. 1. The error bars represent a 95% confidence interval

minimum of 5% observations in the bin). Afterwards, the total O^+ escape flux was estimated for the 9 P_{dyn} subsets and the tendency clearly shows a correlation between the O^+ outflow and P_{dyn} (Fig. 2). The error bars correspond to 95% confidence intervals and are estimated, for each subset (represented as black dots filled in red), from the average O^+ outflow per layer. As an example, the first dot representing the lowest P_{dyn} at $10^{24.6}$ s^{-1} in Fig. 2 contains the average O^+ outflow observations from the layers shown in Fig. 1, subplot 1. Thus, the 95% confidence interval for this subset is given by $CI\,(95\%) = \sqrt{CI^2_{\text{layer1}} + CI^2_{\text{layer2}} + \cdots + CI^2_{\text{layerN}}}$, where $CI_{\text{layer}} = \frac{\sigma * 1.96}{\sqrt{N}}$ with σ the standard deviation of $\log_{10}(O^+$ total flux$)$ in the layer and N the number of O^+ observations in the layer. The same method is applied for the 8 P_{dyn} subsets left. As shown in Fig. 2, the total O^+ escape reaches 1.36×10^{26} s^{-1} for a dynamic pressure of 8.4 nPa. The enhancement of the total O^+ escape rate is about two orders of magnitude meaning that the larger the solar wind dynamic pressure is, the more ions would escape from the plasma mantle.

Furthermore, it is likely that the IMF direction will affect the ion outflow, possibly independent of the geomagnetic activity level (see Additional file 1: Fig. 1). Thus, we investigated O^+ escape for different IMF configurations represented by the clock angle (CA) θ for different dynamic pressure subsets as shown in Fig. 3a. The three dashed curves above the main black curve (labelled no conditions) are for southward IMF or CA $> 90°$. We observed that the more IMF turned southward (CA $> 150°$), the more ions are escaping (see dashed light blue curve). On the contrary, for strong northward

Fig. 3 Interplanetary magnetic field dependency. **a** Total O^+ escape as a function of the solar wind dynamic pressure for the 9 equally distributed subsets with different IMF configurations (clock angle θ—CA). **b** Same plot as plot (**a**) including a 95% confidence interval

IMF (CA $< 30°$) or dotted yellow curve, the total O^+ escape is smaller. The difference between strong northward and strong southward IMF is about 1 order of magnitude. Intermediary curves show the configuration for slightly northward and southward IMF. The dotted dark blue and green curves correspond to northward IMF for $30° < CA < 60°$ and $60° < CA < 90°$, respectively, and the dashed red and pink curves to southward IMF for $90° < CA < 120°$ and $120° < CA < 150°$, respectively. Figure 3b displays the same curves as described but with 95% confidence intervals described above.
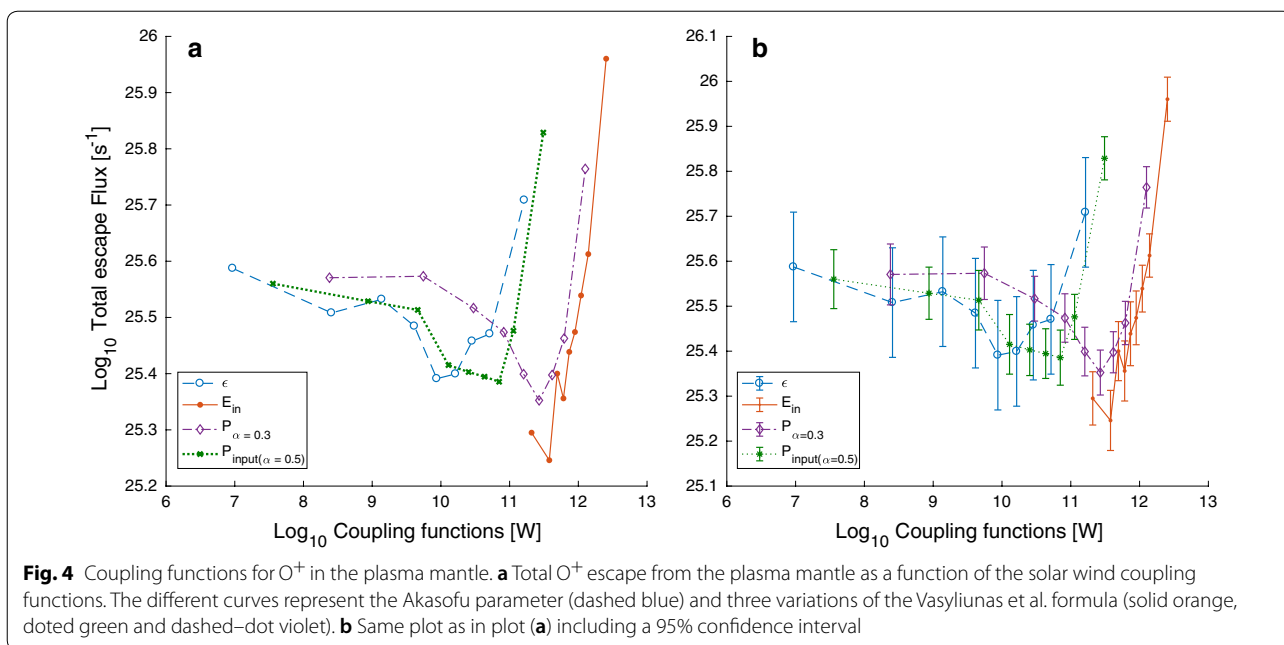
Coupling functions

After the solar wind dynamic pressure, we investigated the solar wind coupling functions because it includes the three previous parameters (n, v and θ) analysed in section Observations. The first coupling function is the Akasofu (or epsilon) parameter, which was initially used to study storms and substorms (Akasofu 1981). As the epsilon parameter is intended for a short period of time, we also estimated three variant formulae of Vasyliunas et al. (1982) for statistics. The four coupling functions investigated for this study are shown in Fig. 4a. This figure gives the total O^+ escape as a function of the coupling functions [W]. The dashed blue curve corresponds to the epsilon parameter, the dotted green one to the Vasyliunas et al. formula with $P_{\mathrm{input}(\alpha=0.5)}$, $F(\theta) = \sin^4(\theta/2)$ (Eq. 2 in the Additional file 1: Tenfjord and Østgaard 2013), the dashed–dotted violet one $P_{\alpha=0.3}$, $F(\theta) = \sin^4(\theta/2)$ (Eq. 1 in the Additional file 1: Finch and Lockwood 2007) and

finally the solid orange to the Vasyliunas et al. formula E_{input} with $\alpha = 0.43$ and $F(\theta) = \sin^{2.7}(\theta/2) + 0.25$ (Eq. 3 in the Additional file 1: Wang et al. 2014a). Figure 4b shows the same coupling functions as described above but with error bars corresponding to a 95% confidence interval (see more details in "Solar wind dynamic pressure and IMF" section).

Similarly to P_{dyn}, the four functions are equally divided into 9 subsets (with the average subsets shown using circles, diamonds, crosses and points on the curves); the first subset corresponds to the average lowest energy input ($\sim 10^7$ W for epsilon and between 10^8 and 10^{11} W for the Vasyliunas et al. formulae) and the last subset to the largest energy input, $\sim 10^{12}$ W. For weak to moderate solar wind energy input or roughly the 5 first subsets, three functions (ϵ, P_α and P_{input}) show a small decrease producing a reduction of O^+ escape flux. For stronger solar wind energy input into the magnetosphere, we observe in the four functions a strong increase in the total O^+ flux (see Fig. 5, zoom of Fig. 4 for higher energy input). However, the 95% confidence intervals of the Akasofu parameter overlap except for the last subset. Consequently, no clear correlation between this parameter and the O^+ escape can be claimed.

Extreme ultraviolet flux

As a complement to the coupling functions, we compare the EUV intensity and EUV flux from the TIMED data with the oxygen data from Cluster. Figure 6a displays the total O^+ escape as a function of the solar wind dynamic pressure for different EUV (intensity, see

Fig. 4 Coupling functions for O^+ in the plasma mantle. **a** Total O^+ escape from the plasma mantle as a function of the solar wind coupling functions. The different curves represent the Akasofu parameter (dashed blue) and three variations of the Vasyliunas et al. formula (solid orange, doted green and dashed–dot violet). **b** Same plot as in plot (**a**) including a 95% confidence interval
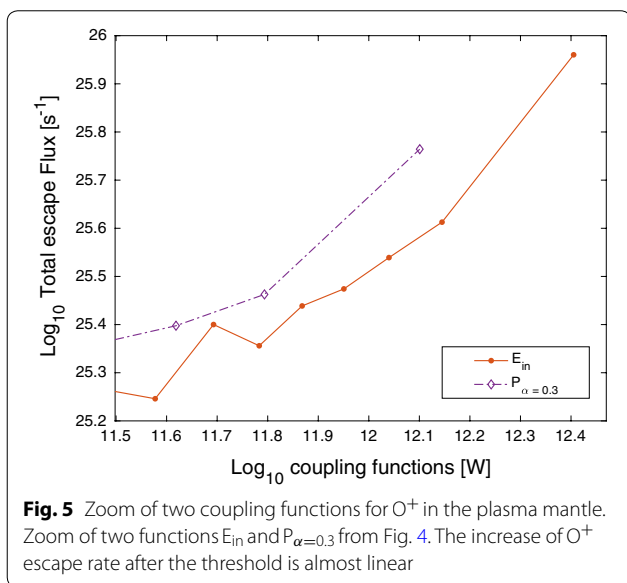
Fig. 5 Zoom of two coupling functions for O^+ in the plasma mantle. Zoom of two functions E_{in} and $P_{\alpha=0.3}$ from Fig. 4. The increase of O^+ escape rate after the threshold is almost linear

Eq. 5) conditions, namely low EUV (dashed blue curve) and high EUV (dotted green curve). Note that the limit between low and high EUV is given by its mean at 0.0035 W/m^2 and the solid dark curve has no EUV conditions (same as in Fig. 2). Figure 6b is identical to Fig. 6a with error bars corresponding to a 95% confidence interval. Our observations show that EUV has a very limited influence, if any, on the total O^+ escape in the plasma mantle.
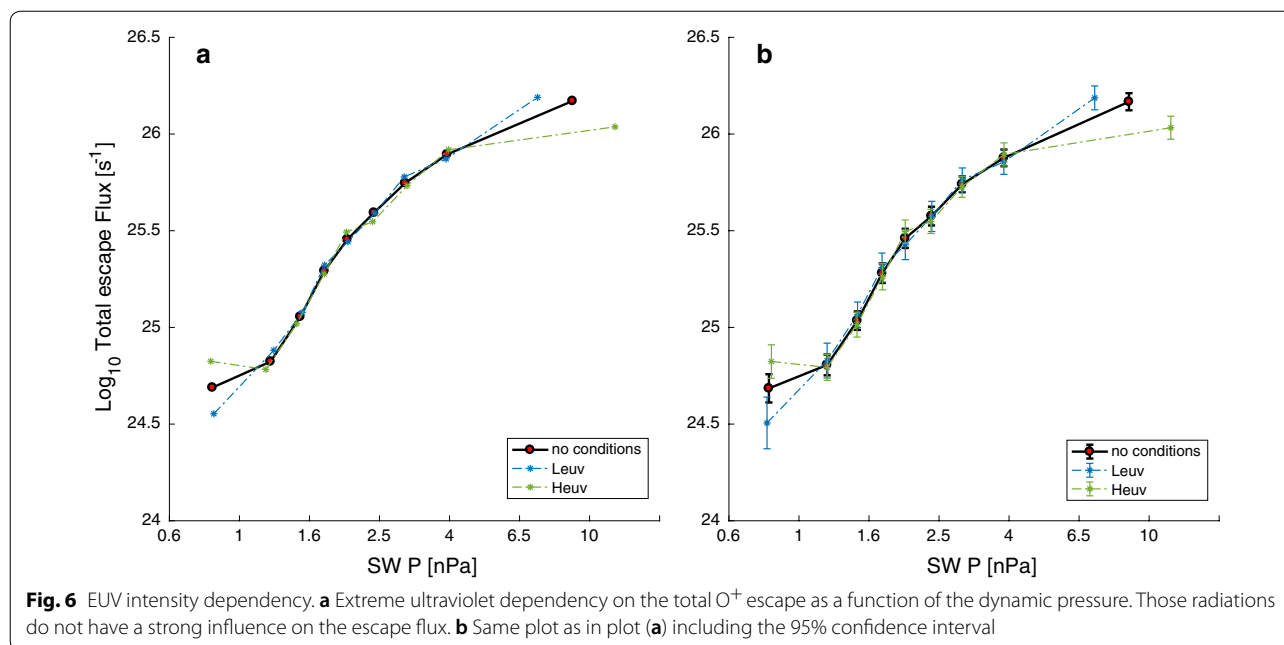
Discussion

Compression of the magnetosphere and solar dynamic pressure

The magnetospheric dynamics is strongly influenced by changing solar wind conditions. During solar storms or long periods of southward IMF, the magnetosphere is compressed. This magnetospheric compression can be observed in Fig. 1 for high dynamic pressure (subplot 9). The O^+ average bins represented in this figure do not fill up the last layer between 10 Re and 11 Re ($\sim 50\%$ less observations than for 8 others subplots). Thus, we interpret a compression of the magnetopause located near 10 Re. On the other hand, for quiet conditions, the average O^+ bins outside the layers (see Fig. 1, subplots 3, 4, 5 for example), which physically means O^+ ions in the magnetosheath (because the magnetopause in quiet conditions is estimated around 10 Re to 11 Re), are discarded in the estimation of the total O^+ escape rate. Thus, in the total O^+ estimation, the escaping area of the filled layers in Fig. 1 includes this compression effect.

We believe that most of the O^+ outflow from the plasma mantle is escaping and lost into the solar wind. Therefore, in this study we replace the total O^+ *outflow* by total O^+ *escape rate*. This statement can be discussed using the ion convection towards the plasma sheet (perpendicular bulk velocity) and the parallel bulk velocity of the ions. Slapak and Nilsson (2018) calculated a convection speed in the plasma mantle of 35 km/s during extreme geomagnetic storms and a corresponding typical parallel ion speed of

Schillings *et al. Earth, Planets and Space* (2019) 71:70

Page 9 of 13

Fig. 6 EUV intensity dependency. **a** Extreme ultraviolet dependency on the total O^+ escape as a function of the dynamic pressure. Those radiations do not have a strong influence on the escape flux. **b** Same plot as in plot (**a**) including the 95% confidence interval

115 km/s, such that these ions reach the plasma sheet ($Z_{GSM} = 0$) at around 50 Re downtail. Under disturbed conditions, those ions are then tailward of the near-Earth neutral sheet X-line (Nagai et al. 1994, 1998) and the O^+ ions will be lost in the distant magnetotail. For more general conditions, Nilsson (2011) found that the average parallel velocity in the mantle was 70 km/s, with a perpendicular temperature of 1 keV. Our ion trajectories for the plasma mantle pass $X_{GSM} = 0$ at an altitude typically above 12 Re, and an average convection velocity towards the plasma sheet for southward IMF is 10 km/s (Haaland et al. 2008). A simple estimate of the transport time from 12 Re to the centre of the plasma sheet would thus be $(12 \times 6371)/10 \simeq 7600$ s, yielding a tailward field-aligned transport of 70 km/s $\times$ 7600 s $\approx$ 80 Re. Here we did not take into account the mirror force acting on the 1 keV average perpendicular temperature, any further ion heating nor any centrifugal acceleration. We thus confirm the conclusions of Nilsson (2011); Nilsson et al. (2012) that most of the cusp/plasma mantle ion outflow will escape.

Our result in Fig. 2 shows a clear correlation between the O^+ escape rate and the solar wind dynamic pressure. A similar trend has been observed by Elliott et al. (2001), who found that in the high-altitude polar cap, the O^+ density and parallel flux increases with solar dynamic pressure. Another aspect influencing the O^+ escape is the IMF direction [here studied through several clock angles (CA)] shown in Fig. 3. Our estimation shows that the O^+ escape rate is higher by a factor of 3 for southward IMF than for northward IMF. Despite that Elliott et al. (2001) did not see any influence of the IMF direction on the O^+

density and parallel flow at high altitudes, this trend was observed by Marcucci et al. (2004) for magnetosheath O^+ ions having higher velocities during southward IMF. Finally, the cusp area increases (Newell and Meng 1994) and moves towards lower latitudes (Palmroth et al. 2001) under larger solar wind pressure and IMF B_z, which also contributes to a higher O^+ escape rate. So, our results are in line with what we expected for O^+ ions in the plasma mantle.

The coupling functions

The coupling functions are defined by the epsilon parameters and the Vasyliunas et al. formula. They are employed for quantifying the energy transferred from the solar wind through the magnetosphere (for further details see Akasofu 1981; Koskinen and Tanskanen 2002 and references therein). In this study, we chose to implement the Akasofu parameter and three variations of the Vasyliunas et al. formula (Eq. 4) with different coupling coefficient α. Note that more details about the three varied equations are given in the Additional file 1.

For a transferred power into the magnetosphere of approximately 10^{10} W, we estimated an O^+ escape rate of 9.13×10^{25} s^{-1} for the Vasyliunas et al. formulae and 5.11×10^{25} s^{-1} for the Akasofu parameter. In comparison, Li et al. (2017) analysed the epsilon parameter for cold ion outflow. The authors used 10 years of Cluster data and estimated the Akasofu parameter under several solar wind parameters. They found that the total cold ion flux is increasing for higher ϵ (up to 10^{11} W). This result (Li et al. 2017) is in agreement with ours as our

epsilon values is estimated in average to 3.05×10^{10} W (see dashed blue curve in Fig. 4) and goes up to 10^{12} W for a few values (see Fig. 5). According to Akasofu (1981), a transferred power of 10^{12} W or higher corresponds to a magnetic storm. From our observations, this statement implies that for geomagnetic storms the O^+ escape rate increases, which is in good agreement with the results found by Schillings et al. (2017, 2018). In addition, we observe a slightly higher solar energy transfer into the magnetosphere during strong southward IMF (up to -30 nT, not shown); meanwhile, the cusp is expanding and moving equatorward (Newell et al. 1989; Palmroth et al. 2001; Li et al. 2012). Therefore, during more intense southward IMF, the interaction area for the penetrating solar wind expands and powers significantly the magnetospheric dynamics.

The most striking feature with all the different coupling functions is that the energy input must reach a certain threshold before any significant change of the O^+ escape rate is seen. After that, there is a strong correlation between any of the coupling functions and the O^+ escape rate. At lower energy input, there is no or even a negative correlation. A possible interpretation is that for low to intermediate energy input, the initial upflow is mainly determined by the solar wind precipitation into the upper atmosphere (Nilsson et al. 1996; Ogawa et al. 2009). As energy input increases, the O^+ escape rate increases and may be due to an expansion of the polar cap and ion circulation to lower latitudes, which results in denser plasma from lower latitude moving towards higher latitudes into the cusp. With the available data we have, this is only a speculation, but it can be tested using ground-based data such as incoherent scatter radars.

Extreme ultraviolet

The low-energy O^+ density and outflow in the polar cap, cusp and lobes have been observed to be dependent of EUV radiation ($F_{10.7}$) (Young et al. 1982; Yau et al. 1988; Cully et al. 2003; André et al. 2015). Despite this, we observe no correlation between the EUV intensity and the O^+ escape rate in the plasma mantle (see Fig. 6). As an extra caution, we tested the EUV dependence for polar cap data using our code and obtained a similar result to the papers cited above (not shown). EUV radiations have an impact in the ionosphere between roughly 80 and 600 km, the ionisation of atomic oxygen to O^+ ions increases at those altitudes, and the O^+ density extends in altitude. On the other hand, all those newly formed ions are not transversely heated and accelerated enough to reach the plasma mantle. One portion will remain bound by gravity, and another portion will become outflow and end up in the plasma sheet. It seems that the amount that reaches the plasma mantle is not strongly dependent on this initial production of ions. This may be because the O^+ in the plasma mantle mainly originates from the ionospheric cusp, where there is also significant soft electron
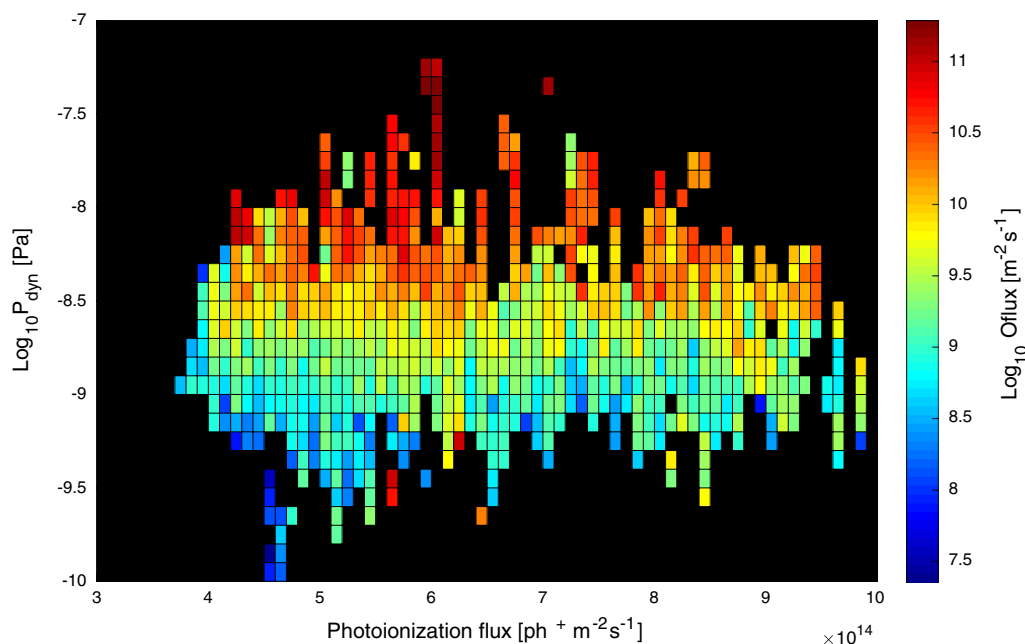
Fig. 7 Photoionisation flux. O^+ outflow in the plasma mantle (colour bar) for different solar wind dynamic pressure and different photoionisation fluxes

precipitation to heat and ionise the ionospheric F-region, leading to the initial upflow (Nilsson et al. 1996; Ogawa et al. 2009); see also statistical maps of electron precipitation (Newell et al. 2009). To strengthen this result, we implemented the O^+ flux as a function of both EUV flux (see Eq. 6) and dynamic pressure (see Fig. 7). We see that, in the plasma mantle, the O^+ escape rate definitely depends on the solar wind dynamic pressure and not on the photoionisation flux (neither does the Kp index see Additional file 1: Fig. 1).

Conclusions

Previous work has reported O^+ outflow dependency with solar wind parameters such as IMF (Slapak et al. 2015), EUV (Yau et al. 1988; Cully et al. 2003; Mouikis et al. 2010) or among other parameters e.g. Abe et al. (1996), Elliott et al. (2001), Lennartsson et al. (2004). However, those results do not cover the plasma mantle region. In this study, we analysed the O^+ escape rate in the plasma mantle for different solar wind parameters, namely the dynamic pressure P_{dyn}, IMF through the clock angle and the EUV flux. We found that

1. The O^+ that will eventually escape from the plasma mantle increase with the solar wind dynamic pressure by about 2 orders of magnitude between the lowest to highest dynamic pressure conditions.
2. The IMF has a clear influence on the O^+ escape with an increase by a factor 3 between northward and southward IMF,
3. The photoionisation flux (EUV flux) does not influence the O^+ escape rate in the plasma mantle.

Our results imply that the higher the O^+ escape rate is, the higher solar wind flux and energy penetrates into the magnetosphere. Therefore, atmospheric loss through the plasma mantle strongly depends on solar wind conditions but not solar radiation. When using a solar wind coupling function, the response is nonlinear and starts to increase only after some threshold is reached. Thus, if we consider higher solar energy input as extreme solar wind conditions, we suggest as a possible explanation that the O^+ escape rate increases significantly due to an increased polar cap size and increased convection of fresh plasma into the ionospheric upflow region. Finally, considering that the young Sun had stronger solar wind, we await that O^+ escape driven by solar wind conditions has a crucial influence on the evolution of the Earth's atmosphere. Therefore, questions remain open and could be addressed in future studies regarding how does the intrinsic magnetic field protect the Earth from significant solar wind penetration and our atmosphere from atmospheric loss.

Additional file

Additional file 1. The first paragraph of the Additional file 1 provides more details on the calculations of the Vasyliunas et al. formula used in Figs. 4 and 5. The equations are fully described. The second part provides additional information on the geomagnetic activity (Kp) compared with the solar wind dynamic pressure and the photoionisation flux.

Authors' contributions
AS made all the plots and main analysis of this study. RS provided the initial code that was used for the analysis. HN, RS, YM, ID and LGW actively participated in the discussions and analysis of the data as well as contributed to the writing of this paper. All authors read and approved the final manuscript.

Author details
[1] Swedish Institute of Space Physics, Kiruna, Sweden. [2] Division of Space Technology, Luleå University of Technology, Kiruna, Sweden. [3] EISCAT Scientific Association, Kiruna, Sweden. [4] IRAP, Université de Toulouse, CNRS, UPS, CNES, Toulouse, France. [5] Division of Fluid and Experimental Mechanics, Luleå University of Technology, Luleå, Sweden.

References
Abe T, Watanabe S, Whalen BA, Yau AW, Sagawa E (1996) Observations of polar wind and thermal ion outflow by Akebono/SMS. J Geomagn Geoelectr 48(3):319–325. https://doi.org/10.5636/jgg.48.319
Akasofu S-I (1981) Energy coupling between the solar wind and the magnetosphere. Space Sci Rev 28(2):121–190. https://doi.org/10.1007/BF00218810
André M, Li K, Eriksson AI (2015) Outflow of low-energy ions and the solar cycle. J Geophys Res Space Phys 120(2):1072–1085. https://doi.org/10.1002/2014JA020714
Axford WI (1968) The polar wind and the terrestrial helium budget. J Geophys Res 73:6855–6859. https://doi.org/10.1029/JA073i021p06855
Balogh A, Carr CM, Acuña MH, Dunlop MW, Beek TJ, Brown P, Fornaçon K-H, Georgescu E, Glassmeier K-H, Harris J, Musmann G, Oddy T, Schwingenschuh K (2001) The Cluster magnetic field investigation: overview of in-flight performance and initial results. Ann Geophys 19:1207–1217. https://doi.org/10.5194/angeo-19-1207-2001
Bouhram M, Klecker B, Miyake W, Rème H, Sauvaud J-A, Malingre M, Kistler L, Blăgău A (2004b) On the altitude dependence of transversely heated O^+ distributions in the cusp/cleft. Ann Geophys 22(5):1787–1798. https://doi.org/10.5194/angeo-22-1787-2004

Chandler MO, Waite JH, Moore TE (1991) Observations of polar ion outflows. J Geophys Res Space Phys 96(A2):1421–1428. https://doi.org/10.1029/90JA02180

Chappell CR, Moore TE, Waite JH Jr (1987) The ionosphere as a fully adequate source of plasma for the Earth's magnetosphere. J Geophys Res 92:5896–5910. https://doi.org/10.1029/JA092iA06p05896

Cully CM, Donovan EF, Yau AW, Arkos GG (2003) Akebono/Suprathermal Mass Spectrometer observations of low-energy ion outflow: dependence on magnetic activity and solar wind conditions. J Geophys Res Space Phys 108:1093. https://doi.org/10.1029/2001JA009200

Denton MH, Taylor MGGT (2008) Solar wind dependence of ion parameters in the Earth's magnetospheric region calculated from cluster observations. Ann Geophys 26(3):387–394. https://doi.org/10.5194/angeo-26-387-2008

Elliott HA, Comfort RH, Craven PD, Chandler MO, Moore TE (2001) Solar wind influence on the oxygen content of ion outflow in the high-altitude polar cap during solar minimum conditions. J Geophys Res Space Phys 106(A4):6067–6084. https://doi.org/10.1029/2000JA003022

Engwall E, Eriksson AI, Cully CM, André M, Puhl-Quinn PA, Vaith H, Torbert R (2009) Survey of cold ionospheric outflows in the magnetotail. Ann Geophys 27(8):3185–3201. https://doi.org/10.5194/angeo-27-3185-2009

Escoubet CP, Fehringer M, Goldstein M (2001) Introduction the Cluster mission. Ann Geophys 19:1197–1200. https://doi.org/10.5194/angeo-19-1197-2001

Finch I, Lockwood M (2007) Solar wind-magnetosphere coupling functions on timescales of 1 day to 1 year. Ann Geophys 25(2):495–506

Gou XC, Shi QQ, Tian AM, Sun WJ, Dunlop MW, Fu SY, Zong QG, Facskó G, Nowada M, Pu ZY, Mailyan B, Xiao T, Shen XC (2016) Solar wind plasma entry observed by cluster in the high-latitude magnetospheric lobes. J Geophys Res Space Phys 121(5):4135–4144. https://doi.org/10.1002/2015JA021578

Green JL, Waite JH Jr (1985) On the origin of polar ion streams. Geophys Res Lett 12:149–152. https://doi.org/10.1029/GL012i003p00149

Güdel M (2007) The sun in time: activity and environment. Living Rev Sol Phys 4:3. https://doi.org/10.12942/lrsp-2007-3. arXiv:0712.1763

Haaland S, Paschmann G, Förster M, Quinn J, Torbert R, Vaith H, Puhl-Quinn P, Kletzing C (2008) Plasma convection in the magnetotail lobes: statistical results from cluster edi measurements. Ann Geophys 26(8):2371–2382. https://doi.org/10.5194/angeo-26-2371-2008

Haaland S, Lybekk B, Maes L, Laundal K, Pedersen A, Tenfjord P, Ohma A, Østgaard N, Reistad J, Snekvik K (2017) North–south asymmetries in cold plasma density in the magnetotail lobes: Cluster observations. J Geophys Res Space Phys 122(1):136–149. https://doi.org/10.1002/2016JA023404

Kistler LM, Mouikis CG (2016) The inner magnetosphere ion composition and local time distribution over a solar cycle. J Geophys Res Space Phys 121(3):2009–2032. https://doi.org/10.1002/2015JA021883

Kistler LM, Mouikis CG, Cao X, Frey H, Klecker B, Dandouras I, Korth A, Marcucci MF, Lundin R, McCarthy M, Friedel R, Lucek E (2006) Ion composition and pressure changes in storm time and nonstorm substorms in the vicinity of the near-Earth neutral line. J Geophys Res Space Phys 111(A10):11222. https://doi.org/10.1029/2006JA011939

Koskinen HEJ, Tanskanen EI (2002) Magnetospheric energy budget and the epsilon parameter. J Geophys Res Space Phys 107(A11):42–14210. https://aurora/doi.org/10.1029/2002JA009283

Kronberg EA, Ashour-Abdalla M, Dandouras I, Delcourt DC, Grigorenko EE, Kistler LM, Kuzichev IV, Liao J, Maggiolo R, Malova HV, Orlova KG, Peroomian V, Shklyar DR, Shprits YY, Welling DT, Zelenyi LM (2014) Circulation of heavy ions and their dynamical effects in the magnetosphere: recent observations and models. Space Sci Rev 184:173–235. https://doi.org/10.1007/s11214-014-0104-0

Kusnierkiewicz DY (2003) An overview of the timed spacecraft. Technical Report 2, JHU/APL Technical Digest

Lennartsson OW, Collin HL, Peterson WK (2004) Solar wind control of Earth's H^+ and O^+ outflow rates in the 15-eV to 33-keV energy range. J Geophys Res Space Phys 109(A18):12212. https://doi.org/10.1029/2004JA010690

Li K, Haaland S, Eriksson A, André M, Engwall E, Wei Y, Kronberg EA, Fränz M, Daly PW, Zhao H, Ren QY (2012) On the ionospheric source region of cold ion outflow. Geophys Res Lett 39:18102. https://doi.org/10.1029/2012GL053297

Li K, Wei Y, André M, Eriksson A, Haaland S, Kronberg EA, Nilsson H, Maes L, Rong ZJ, Wan WX (2017) Cold ion outflow modulated by the solar wind energy input and tilt of the geomagnetic dipole. J Geophys Res Space Phys 122(10):10658–10668. https://doi.org/10.1002/2017JA024642

Li K, Wei Y, Haaland S, Kronberg EA, Rong ZJ, Maes L, Maggiolo R, André M, Nilsson H, Grigorenko E (2018) Estimating the kinetic energy budget of the polar wind outflow. J Geophys Res Space Phys 123(9):7917–7929. https://doi.org/10.1029/2018JA02581

Liao J, Kistler LM, Mouikis CG, Klecker B, Dandouras I, Zhang J-C (2010) Statistical study of O^+ transport from the cusp to the lobes with Cluster CODIF data. J Geophys Res Space Phys 115:00–15. https://doi.org/10.1029/2010JA015613

Liao J, Kistler LM, Mouikis CG, Klecker B, Dandouras I (2015) Acceleration of O^+ from the cusp to the plasma sheet. J Geophys Res Space Phys 120:1022–1034. https://doi.org/10.1002/2014JA020341

Maes L, Maggiolo R, De Keyser J, Dandouras I, Fear RC, Fontaine D, Haaland S (2015) Solar illumination control of ionospheric outflow above polar cap arcs. Geophys Res Lett 42(5):1304–1311. https://doi.org/10.1002/2014GL062972.2014GL062972

Maggiolo R, Kistler LM (2014) Spatial variation in the plasma sheet composition: dependence on geomagnetic and solar activity. J Geophys Res Space Phys 119:2836–2857. https://doi.org/10.1002/2013JA019517

Maggiolo R, Sauvaud J-A, Fontaine D, Teste A, Grigorenko E, Balogh A, Fazakerley A, Paschmann G, Delcourt D, Rème H (2006) A multi-satellite study of accelerated ion beams above the polar cap. Ann Geophys 24(6):1665–1684. https://doi.org/10.5194/angeo-24-1665-2006

Marcucci MF, Bavassano Cattaneo MB, Pallocchia G, Amata E, Bruno R, Di Lellis AM, Formisano V, Rème H, Bosqued JM, Dandouras I, Sauvaud J-A, Kistler LM, Moebius E, Klecker B, Carlson CW, Parks GK, McCarthy M, Korth A, Lundin R, Balogh A (2004) Energetic magnetospheric oxygen in the magnetosheath and its response to IMF orientation: Cluster observations. J Geophys Res Space Phys. https://doi.org/10.1029/2003JA010312

Mouikis CG, Kistler LM, Liu YH, Klecker B, Korth A, Dandouras I (2010) H^+ and O^+ content of the plasma sheet at 15–19 Re as a function of geomagnetic and solar activity. J Geophys Res Space Phys 115:00–16. https://doi.org/10.1029/2010JA015978

Murayama T (1982) Coupling function between solar wind parameters and geomagnetic indices. Rev Geophys 20(3):623–629. https://doi.org/10.1029/RG020i003p00623

Nagai T, Waite JH, Green JL, Chappell CR, Olsen RC, Comfort RH (1984) First measurements of supersonic polar wind in the polar magnetosphere. Geophys Res Lett 11(7):669–672. https://doi.org/10.1029/GL011i007p00669

Nagai T, Takahashi K, Kawano H, Yamamoto T, Kokubun S, Nishida A (1994) Initial geotail survey of magnetic substorm signatures in the magnetotail. Geophys Res Lett 21(25):2991–2994. https://doi.org/10.1029/94GL01420

Nagai T, Fujimoto M, Nakamura R, Saito Y, Mukai T, Yamamoto T, Nishida A, Kokubun S, Reeves GD, Lepping RP (1998) Geotail observations of a fast tailward flow at $\times$ gsm $= -15$ Re. J Geophys Res Space Phys 103(A10):23543–23550. https://doi.org/10.1029/98JA02246

Newell PT, Meng C-I (1994) Ionospheric projections of magnetospheric regions under low and high solar wind pressure conditions. J Geophys Res Space Phys 99:273–286. https://doi.org/10.1029/93JA02273

Newell PT, Sotirelis T, Wing S (2009) Diffuse, monoenergetic, and broadband aurora: the global precipitation budget. J Geophys Res Space Phys. https://doi.org/10.1029/2009JA014326

Newell PT, Meng C-I, Sibeck DG, Lepping R (1989) Some low-altitude cusp dependencies on the interplanetary magnetic field. J Geophys Res Space Phys 94:8921–8927. https://doi.org/10.1029/JA094iA07p08921

Nilsson H, Waara M, Arvelius S, Marghitu O, Bouhram M, Hobara Y, Yamauchi M, Lundin R, Rème H, Sauvaud J-A, Dandouras I, Balogh A, Kistler LM, Klecker B, Carlson CW, Bavassano-Cattaneo MB, Korth A (2006) Characteristics of high altitude oxygen ion energization and outflow as observed by Cluster: a statistical study. Ann Geophys 24:1099–1112. https://doi.org/10.5194/angeo-24-1099-2006

Nilsson H, Waara M, Marghitu O, Yamauchi M, Lundin R, Rème H, Sauvaud J-A, Dandouras I, Lucek E, Kistler LM, Klecker B, Carlson CW, Bavassano-Cattaneo MB, Korth A (2008) An assessment of the role of the centrifugal acceleration mechanism in high altitude polar cap oxygen ion outflow. Ann Geophys 26:145–157. https://doi.org/10.5194/angeo-26-145-2008

Nilsson H, Engwall E, Eriksson A, Puhl-Quinn PA, Arvelius S (2010) Centrifugal acceleration in the magnetotail lobes. Ann Geophys 28:569–576. https://doi.org/10.5194/angeo-28-569-2010

Schillings *et al. Earth, Planets and Space* (2019) 71:70

Page 13 of 13

Nilsson H, Barghouthi IA, Slapak R, Eriksson AI, André M (2012) Hot and cold ion outflow: spatial distribution of ion heating. J Geophys Res Space Phys 117(A16):11201. https://doi.org/10.1029/2012JA017974

Nilsson H (2011) In: Liu W, Fujimoto M (ed) Heavy ion energization, transport, and loss in the Earth's magnetosphere. Springer, Dordrecht, pp 315–327

Nilsson H, Kirkwood S, Bjørnå N (1996) Bistatic measurements of incoherent scatter plasma lines. J Atmos Terr Phys 58(1):175–187. https://doi.org/10.1016/0021-9169(95)00028-3 (**Selected papers from the sixth international Eiscat Workshop**)

Ogawa Y, Buchert SC, Fujii R, Nozawa S, van Eyken AP (2009) Characteristics of ion upflow and downflow observed with the european incoherent scatter svalbard radar. J Geophys Res Space Phys. https://doi.org/10.1029/2008JA013817

Palmroth M, Laakso H, Pulkkinen TI (2001) Location of high-altitude cusp during steady solar wind conditions. J Geophys Res Space Phys 106(A10):21109–21122. https://doi.org/10.1029/2001JA900073

Ramstad R, Barabash S, Futaana Y, Nilsson H, Wang X-D, Holmström M (2015) The Martian atmospheric ion escape rate dependence on solar wind and solar EUV conditions: 1. Seven years of Mars Express observations. J Geophys Res Planets 120(7):1298–1309. https://doi.org/10.1002/2015JE004816

Ramstad R, Barabash S, Futaana Y, Nilsson H, Holmström M (2017) Global mars-solar wind coupling and ion escape. J Geophys Res Space Phys 122(8):8051–8062. https://doi.org/10.1002/2017JA024306

Rème H, Aoustin C, Bosqued JM, Dandouras I, Lavraud B, Sauvaud JA, Barthe A, Bouyssou J, Camus T, Coeur-Joly O, Cros A, Cuvilo J, Ducay F, Garbarowitz Y, Medale JL, Penou E, Perrier H, Romefort D, Rouzaud J, Vallat C, Alcaydé D, Jacquey C, Mazelle C, D'Uston C, Möbius E, Kistler LM, Crocker K, Granoff M, Mouikis C, Popecki M, Vosbury M, Klecker B, Hovestadt D, Kucharek H, Kuenneth E, Paschmann G, Scholer M, Sckopke N, Seidenschwang E, Carlson CW, Curtis DW, Ingraham C, Lin RP, McFadden JP, Parks GK, Phan T, Formisano V, Amata E, Bavassano-Cattaneo MB, Baldetti P, Bruno R, Chionchio G, di Lellis A, Marcucci MF, Pallocchia G, Korth A, Daly PW, Graeve B, Rosenbauer H, Vasyliunas V, McCarthy M, Wilber M, Eliasson L, Lundin R, Olsen S, Shelley EG, Fuselier S, Ghielmetti AG, Lennartsson W, Escoubet CP, Balsiger H, Friedel R, Cao J-B, Kovrazhkin RA, Papamastorakis I, Pellat R, Scudder J, Sonnerup B (2001) First multispacecraft ion measurements in and near the Earth's magnetosphere with the identical Cluster ion spectrometry (CIS) experiment. Ann Geophys 19:1303–1354. https://doi.org/10.5194/angeo-19-1303-2001

Schillings A, Nilsson H, Slapak R, Yamauchi M, Westerberg L-G (2017) Relative outflow enhancements during major geomagnetic storms—Cluster observations. Ann Geophys 35(6):1341–1352. https://doi.org/10.5194/angeo-35-1341-2017

Schillings A, Nilsson H, Slapak R, Wintoft P, Yamauchi M, Wik M, Dandouras I, Carr CM (2018) O $^+$ escape during the extreme space weather event of 4–10 September 2017. Space Weather 16(9):1363–1376. https://doi.org/10.1029/2018SW001881

Shelley EG, Peterson WK, Ghielmetti AG, Geiss J (1982) The polar ionosphere as a source of energetic magnetospheric plasma. Geophys Res Lett 9:941–944. https://doi.org/10.1029/GL009i009p00941

Shue J-H, Song P, Russell CT, Steinberg JT, Chao JK, Zastenker G, Vaisberg OL, Kokubun S, Singer HJ, Detman TR, Kawano H (1998) Magnetopause location under extreme solar wind conditions. J Geophys Res 103:17691–17700. https://doi.org/10.1029/98JA01103

Slapak R, Nilsson H (2018) The oxygen ion circulation in the outer terrestrial magnetosphere and its dependence on geomagnetic activity. Geophys Res Lett 45:12669–12676

Slapak R, Nilsson H, Westerberg LG (2013) A statistical study on O $^+$ flux in the dayside magnetosheath. Ann Geophys 31:1005–1010. https://doi.org/10.5194/angeo-31-1005-2013

Slapak R, Nilsson H, Waara M, André M, Stenberg G, Barghouthi IA (2011) O $^+$ heating associated with strong wave activity in the high altitude cusp and mantle. Ann Geophys 29:931–944. https://doi.org/10.5194/angeo-29-931-2011

Slapak R, Nilsson H, Westerberg LG, Eriksson A (2012) Observations of oxygen ions in the dayside magnetosheath associated with southward IMF. J Geophys Res Space Phys 117:07218. https://doi.org/10.1029/2012JA017754

Slapak R, Nilsson H, Westerberg LG, Larsson R (2015) O $^+$ transport in the dayside magnetosheath and its dependence on the IMF direction. Ann Geophys 33(3):301–307. https://doi.org/10.5194/angeo-33-301-2015

Slapak R, Schillings A, Nilsson H, Yamauchi M, Westerberg I (2017) Atmospheric loss from the dayside open polar region and its dependence on geomagnetic activity: implications for atmospheric escape on evolutionary timescales. Ann Geophys 35:721–731

Stamper R, Lockwood M, Wild MN, Clark TDG (1999) Solar causes of the long-term increase in geomagnetic activity. J Geophys Res Space Phys 104(A12):28325–28342. https://doi.org/10.1029/1999JA900311

Tenfjord P, Østgaard N (2013) Energy transfer and flow in the solar wind–magnetosphere–ionosphere system: a new coupling function. J Geophys Res Space Phys 118(9):5659–5672. https://doi.org/10.1002/jgra.50545

Vasyliunas VM, Kan JR, Siscoe GL, Akasofu S-I (1982) Scaling relations governing magnetospheric energy transfer. Planet Space Sci 30(4):359–365. https://doi.org/10.1016/0032-0633(82)90041-1

Waara M, Slapak R, Nilsson H, Stenberg G, André M, Barghouthi IA (2011) Statistical evidence for O $^+$ energization and outflow caused by wave-particle interaction in the high altitude cusp and mantle. Ann Geophys 29:945–954. https://doi.org/10.5194/angeo-29-945-2011

Wang C, Han JP, Li H, Peng Z, Richardson JD (2014a) Solar wind–magnetosphere energy coupling function fitting: results from a global MHD simulation. J Geophys Res Space Phys 119(8):6199–6212. https://doi.org/10.1002/2014JA019834

Wang CP, Lyons LR, Angelopoulos V (2014b) Properties of low-latitude mantle plasma in the Earth's magnetotail: ARTEMIS observations and global MHD predictions. J Geophys Res Space Phys 119(9):7264–7280. https://doi.org/10.1002/2014JA020060

Woods TN, Bailey S, Eparvier F, Lawrence G, Lean J, McClintock B, Roble R, Rottman GJ, Solomon SC, Tobiska WK, White OR (2000) Timed solar EUV experiment. Phys Chem Earth Part C Solar Terr Planet Sci 25(5):393–396. https://doi.org/10.1016/S1464-1917(00)00040-4

Yau AW, Peterson WK, Shelley EG (1988) Quantitative parametrization of energetic ionospheric ion outflow. In: Moore TE, Waite Jr JH, Moorehead TW, Hansin WB (eds) Modeling magnetospheric plasma. Geophysical Monograph Series, vol 44. American Geophysical Union, Washington, DC, pp 211–217. https://doi.org/10.1029/GM044p0211

Yau AW, Abe T, Peterson WK (2007) The polar wind: recent observations. J Atmos Solar Terr Phys 69(16):1936–1983. https://doi.org/10.1016/j.jastp.2007.08.010 (**Recent Advances in the Polar Wind Theories and Observations**)

Young DT, Balsiger H, Geiss J (1982) Correlations of magnetospheric ion composition with geomagnetic and solar activity. J Geophys Res Space Phys 87(A11):9077–9096. https://doi.org/10.1029/JA087iA11p09077

Publisher's Note